Chin. Phys. Lett. **39**, 058501 (2022)

Highly Sensitive Mid-Infrared Photodetector Enabled by Plasmonic Hot Carriers in the First Atmospheric Window

Yuan-Fang Yu(于远方)[1], Ye Zhang(张也)[2], Fan Zhong(仲帆)[2], Lin Bai(白琳)[1], Hui Liu(刘辉)[2], Jun-Peng Lu(吕俊鹏)[1*], and Zhen-Hua Ni(倪振华)[1*]

[1]*School of Physics, Southeast University, Nanjing 211189, China*
[2]*National Laboratory of Solid State Microstructures & School of Physics, Collaborative Innovation Center of Advanced Microstructures, Nanjing University, Nanjing 210093, China*

(Received 3 March 2022; accepted 28 March 2022; published online 26 April 2022)

The first atmospheric window of 3–5 μm in the mid-infrared (MIR) spectral range pertains to crucial application fields, with particular scientific and technological importance. However, conventional narrow-bandgap semiconductors operating at this band, represented by mercury cadmium telluride and indium antimonide, suffer from limited specific detectivity at room temperature and hindered optoelectronic integration. In this study, a plasmonic hot electron-empowered MIR photodetector based on Al-doped ZnO (AZO)/bi-layer graphene heterostructure is demonstrated. Free electrons oscillate coherently in AZO disk arrays, resulting in strong localized surface plasmon resonance (LSPR) in the MIR region. The photoelectric conversion efficiency at 3–5 μm is significantly improved due to plasmon-induced hot-electron extraction and LSPR-enhanced light absorption. The specific detectivity reaches about 1.4×10^{11} Jones and responsivity is up to 4712.3 A/W at wavelength of 3 μm at room temperature. The device's specific detectivity is among the highest performance of commercial state-of-the-art photodetectors and superior to most of the other 2D materials based photodetectors in the MIR region. These results demonstrate that a plasmonic heavily doped metal oxides/2D material heterostructure is a suitable architecture for constructing highly sensitive room-temperature MIR photodetectors.

DOI: 10.1088/0256-307X/39/5/058501

Mid-infrared (MIR) photodetectors for the first atmospheric window of 3–5 μm are highly significant for advanced applications, such as remote sensing,[1] communications,[2] and astronomy.[3] Conventional MIR devices based on epitaxially grown narrow-bandgap semiconductors, such as mercury cadmium telluride (MCT) and indium antimonide, still encounter challenges of limited detectivity at room temperature and hindered optoelectronic integration.[4,5] The high dark current of MCT photodetectors can result in increased noise, e.g., the generation–recombination noise makes it difficult to achieve high-performance MIR detection without a cryogenic environment. Moreover, complex cooling facilities severely hinder the optoelectronic integration of MCT in applications.[4] Graphene has recently attracted widespread interest in room-temperature photodetection due to its unique properties, such as high carrier mobility and broadband light absorption in ultraviolet-to-THz region.[6] Further, atomic thickness and the absence of dangling bonds make it easy for graphene to form van der Waals heterojunctions and on-chip optoelectronic integration.[7–9] However, intrinsic graphene photodetectors always suffer from low sensitivity, mainly due to weak light absorption[10] and short carrier lifetime.[11]

Integrating plasmonic nanostructures into devices is an effective approach for photoelectric performance improvement, in which the induced near-field enhancement can prominently strengthen the light-harvesting capability of active materials.[12] In addition, localized surface plasmon resonances (LSPR) in nanostructures can damp nonradiatively by generating hot carriers via Landau damping.[13] The hot carrier harvesting before relaxation can prevent excess energy dissipation and carrier loss, resulting in efficient photoelectric conversion.[14] The issue of bandgap-limited spectral response range in infrared photon detectors can be addressed by hot carrier transfer.[15] Beyond noble metals, heavily doped metal oxides, such as Sn-doped In_2O_3 (ITO) and AZO, are excellent platforms for infrared plasmonic optoelectronics with low optical losses, which have composition-dependent LSPR ranging in near-infrared-to-MIR region.[16–18]

In this study, we demonstrate a plasmonic hot carrier-enabled MIR photodetector based on AZO/bi-layer graphene heterostructure, which exhibits high detectivity at the first atmospheric window. Under MIR light illumination, free electrons at the conduction band of AZO are excited to a high energy level as energetic hot electrons, with LSPR damping. Ultrafast hot-electron transfer can overwhelm the competitive intraband cooling and prevent energy dis-

*Corresponding author. Email: phyljp@seu.edu.cn; zhni@seu.edu.cn
© 2022 Chinese Physical Society and IOP Publishing Ltd

sipation, improving the efficiency of infrared photoelectric conversion. Attributed to hot-electron transfer and improved light absorption, the AZO/bi-layer graphene hybrid devices exhibit a high detectivity of about 1.4×10^{11} Jones and responsivity of about 4712.3 A/W at 3 μm at room temperature, which is superior to most 2D material-based MIR photodetectors, and nearly one order of magnitude higher than that in commercial MCT. These results demonstrate that constructing heterostructures with 2D materials and plasmonic heavily doped metal oxides are a suitable strategy for realizing on-chip integration of room-temperature MIR photodetectors.

LSPR in AZO Arrays in MIR Region. To fabricate the AZO arrays, a poly(methyl methacrylate) (PMMA) layer was spin-coated on a SiO_2/Si substrate. Microhole arrays were patterned in the PMMA layer with standard lithography procedures. AZO (Al:ZnO = 2:98) is sequentially deposited on the patterned PMMA film by thermal evaporation. Then, a lift-off process is implemented to remove PMMA with acetone, and the sample is annealed in a vacuum under 135 ℃ for an hour to improve the crystallinity.

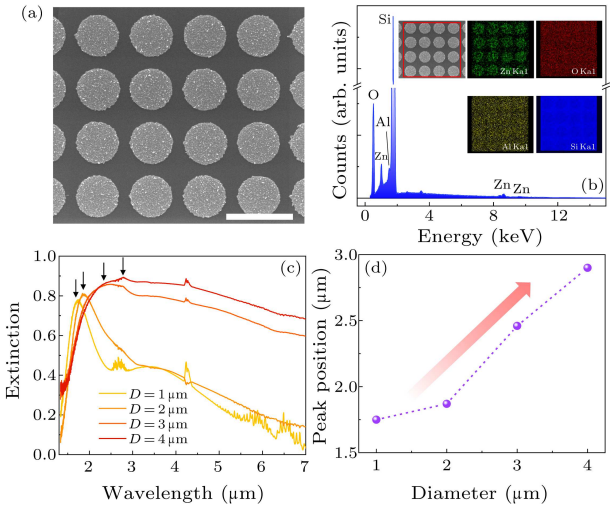

Fig. 1. LSPR in AZO arrays in the MIR region. (a) SEM image of prepared periodical AZO arrays with the thickness of about 100 nm (scale bar 5 μm). (b) EDS spectrum of AZO on the SiO_2/Si substrate. Insets: SEM and EDS maps of AZO arrays. The images with false colors correspond to the elements: Zn (green), O (red), Al (yellow), and Si (blue). (c) Extinction spectra of the annealed periodical AZO arrays with different diameters (1 to 4 μm) and the same edge-to-edge separation of 1 μm. (d) The peak position of LSPR as a function of diameter.

Figure 1(a) shows the scanning electron microscope (SEM) image of AZO micro-disk arrays on the SiO_2/Si substrate with a period of 4 μm and diameter of 3 μm. The thickness of the AZO micro-disk is about 100 nm (Fig. S1 in the Supporting Information). Energy-dispersive x-ray spectroscopy (EDS) and mapping were performed to identify the elemental composition of AZO arrays [Fig. 1(b)]. Al doping and the creation of oxygen vacancies can dramatically increase the free carrier concentration in AZO, thus increasing the Fermi level beyond the edge of the conduction band.[16] The coherent oscillation of free electrons in the AZO array supports a strong LSPR in the MIR region (approximately ranging from about 1.5 to 7 μm),[18] which is characterized using Fourier transform infrared spectroscopy [Fig. 1(c)]. As is expected, the resonance peak of the AZO disk shifts to longer wavelengths when the disk diameter increases, due to the reduced restoring force in the system [Fig. 1(d)], which is consistent with the behavior of LSPR-induced light absorption.[19]

Photoelectric Conversion Mechanisms in AZO/bi-layer Graphene Heterostructure. Photodetectors based on AZO/bi-layer graphene heterostructure were fabricated [Fig. 2(a)]. Bi-layer graphene was mechanically exfoliated from highly oriented pyrolytic graphite and transferred onto a Si substrate with a 300-nm-thick SiO_2 capping layer. The Au electrodes (about 50 nm) with a Ni adhesion layer (about 5 nm) were fabricated via a standard lithography procedure using electron beam lithography, thermal evaporation, and lift-off procedures. Then, the AZO arrays are directly fabricated on the graphene channel. The output characteristic curve measured under dark conditions reveals the ohmic contact of the device, which ensures the effective collection of photogenerated carriers [Fig. 2(b)].[20] After the heterostructure formation, holes can transfer from AZO to graphene until an equilibrium state is reached, resulting in the p-doping of graphene. Under MIR illumination, free electrons at the conduction band of AZO can be excited to a high energy level as energetic hot electrons via LSPR damping,[21] and then enter the graphene channel, as depicted in Fig. 2(c). Ultrafast hot-electron transfer can overwhelm the competitive cooling process and prevent energy dissipation, thus improving the efficiency of infrared photoelectric conversion. Meanwhile, photogenerated holes are trapped in AZO with a certain spatial distribution, producing an additional electric field as a local gate voltage to modulate the channel conductance.[8] The devices have significant photoconductive gain due to the gating effects and hole trapping that prolong the carrier lifetime. The avoided energy dissipation by hot-electron transfer and the photogain mechanisms synchronously give the MIR AZO/bi-layer graphene photodetectors a high detectivity.

Raman spectra of the bi-layer graphene and plasmonic AZO/bi-layer graphene heterostructure were obtained to verify the charge-doping scenario when forming heterostructures [Fig. 2(d)]. After forming heterostructures, the in-plane vibrational G-band of graphene blueshift from 1580 to 1582 cm^{-1} (Fig. S2) indicates the occurrence of charge doping due to the nonadiabatic removal of the Kohn anomaly at the Γ point. The blueshift of the 2D band from 2686 to 2690 cm^{-1} after coupling with AZO (Fig. S3) demon-

strates that graphene is doped by holes due to the charge-transfer-induced modification of the equilibrium lattice parameter.[22–24]

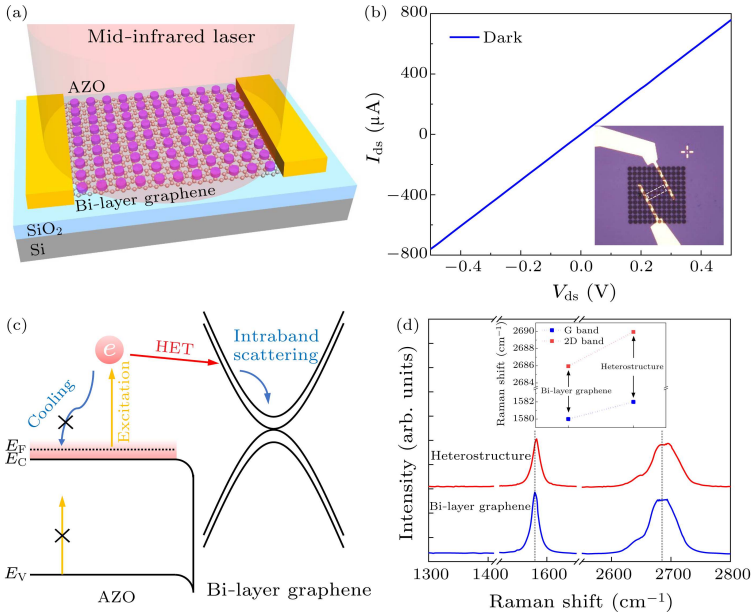

Fig. 2. Photoelectric conversion mechanisms in the AZO/bi-layer graphene photodetector. (a) The schematic illustration of the device architecture. (b) The output characteristic curve measured under dark conditions for $V_g = 0$ V. Inset at the bottom right is the optical image of the prepared device. (c) Schematic illustration of band diagrams, the excitation of plasmon-induced hot electrons under MIR laser excitation (yellow arrow), blocked interband transition under sub-bandgap excitation (yellow arrow with a black fork), hot-electron transfer (red arrow), the avoided carrier cooling (blue bending line), and intraband scattering in graphene (blue arc-shaped line). (d) Raman spectra acquired from AZO/bi-layer graphene heterostructure and pristine bi-layer graphene. Inset shows the Raman shift changes of the G and 2D bands of graphene before and after coupling with plasmonic AZO disk arrays. The wavelength of the excited laser is 532 nm, with a laser power of 400 μW.

Highly Sensitive Mid-Infrared Photodetection Enabled by Plasmonic Hot Carriers. The photoresponse of an AZO/bi-layer graphene hybrid photodetector under 3, 3.5, and 4 μm excitation is further characterized. The hybrid device, dominated by hot-electron transfer, shows dramatic photoresponse at room temperature [Fig. 3(a)]. Moreover, the response wavelengths ranging from 2.8 to 4 μm are consistent with the broadband LSPR profile at MIR [Fig. 3(b)]. We calculated the essential parameters of the AZO/bi-layer graphene photodetector to evaluate the device's performance. The detectivity D^* can be calculated using the equation[25]

$$D^* = \frac{R\sqrt{A}}{\sqrt{2eI_{\text{dark}}}}, \tag{1}$$

where R is the responsivity, A is the effective area of the device, e is the electron charge, and I_{dark} is the dark current. Figure 3(c) shows that the maximum D^* and responsivity of the AZO/bi-layer graphene device reach about 1.4×10^{11} Jones and 4712.3 A/W at 3 μm, respectively. The device also exhibits comparable sensitivity at the wavelengths of 3.5 and 4 μm, which can be attributed to AZO's broad and robust MIR LSPR (Fig. S4). Under 3.5 μm illumination, the maximum D^* and R are as high as 4.2×10^{10} Jones and 1481.7 A/W, respectively. Further, the device still maintains a high sensitivity under 4 μm illumination, with the maximum D^* and R of about 1.4×10^{10} Jones and 477.9 A/W, respectively. We have also calculated the device's external quantum efficiency (EQE) using the equation[26]

$$\text{EQE} = \frac{Rhc}{e\lambda}, \tag{2}$$

where R is the responsivity, e is the elemental charge, h is the Planck constant, c is the speed of light in vacuum, and λ is the frequency of light. Figure S5 in the Supporting Information shows that the EQE of the device can reach about 194750%, 52490%, and 14810% at the wavelengths of 3, 3.5, and 4 μm, respectively, due to the effective hot-electron harvesting and photogain mechanisms. Notably, the high D^*, responsivity, and EQE can be further tuned by varying the ratio of the doped Al atoms, which significantly impacts the free carrier concentration and the MIR LSPR character.

Another essential parameter of the photodetector is the response time. Curve fitting using the following double exponential functions extracts the rise time (τ_1, τ_2) and decay time (τ_3, τ_4) of the AZO/bi-layer graphene photodetector:

$$I_{\text{ph}} = A_1 \exp(-t/\tau_1) + A_2 \exp(-t/\tau_2), \tag{3}$$

$$I_{\text{ph}} = A_3 \exp(-t/\tau_3) + A_4 \exp(-t/\tau_4). \tag{4}$$

According to the fitting results, the photoresponse of our devices at 3.5 μm is divided into two processes [Fig. 3(d)], in which τ_1 is about 1.8 s and τ_2 is about 13.5 s for the photocurrent increase. The decay time constant τ_3 is about 3.1 s and τ_4 is about 117.5 s. The relatively slow response is thought to be due to the defects trapping in photogenerated holes in AZO with shallow and deep states, which can extend carrier lifetimes and increase photoconductive gain.[8]

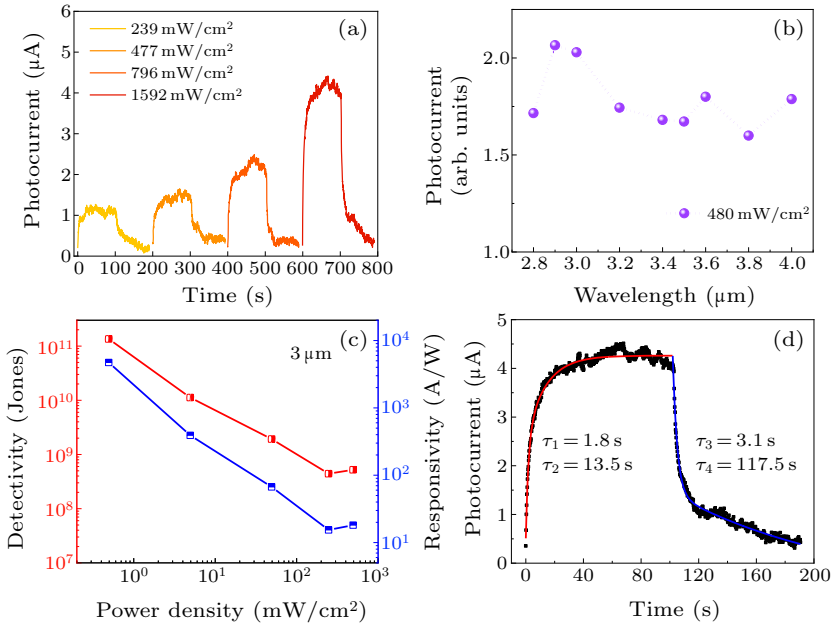

Fig. 3. Photoresponse characterization of the AZO/bi-layer graphene MIR photodetectors at room temperature. $V_{ds} = 0.5$ V and $V_g = 0$ V. (a) Photoresponse of the device under different power densities at a wavelength of 3.5 μm. (b) Photocurrent of the devices as a function of wavelength at a power density of 480 mW/cm^2. (c) Power density-dependent detectivity and responsivity at a wavelength of 3 μm. (d) Transient response of AZO/bi-layer graphene photodetectors. The red and blue solid lines represent the fitting curves based on a double exponential function.

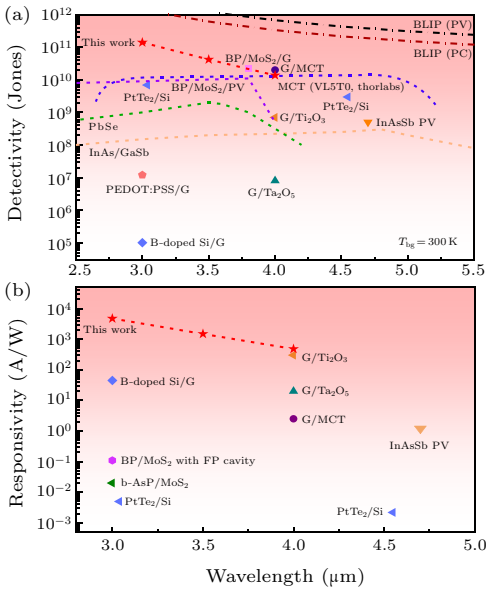

Fig. 4. Performance comparison of the AZO/bi-layer graphene photodetectors with the previously reported photodetectors at room temperature. (a) Comparison of the specific detectivity between AZO/bi-layer graphene photodetector and other devices reported in the literature. Dash-dotted lines show the photovoltaic and photoconductive BLIP calculated for the field of view (FOV = 2π). (b) Comparison of responsivity of the AZO/bi-layer graphene photodetector with other reported MIR devices.

Figures 4(a) and 4(b) show the comparison of the AZO/bi-layer graphene photodetector with other MIR devices reported in literature. The detectivity and responsivity of our device are superior to most of the other advanced photodetectors based on low-dimensional materials,[3,27–31] such as b-AsP/MoS_2,[32] graphene/Ta_2O_5,[33] and B-doped Si/graphene.[34] Notably, the detectivity of the AZO/bi-layer graphene device at 3 μm is one order of magnitude higher than the existing commercial MCT detectors.[35] The highly sensitive, low-cost, and stable AZO/bi-layer graphene photodetector demonstrates significant potential in practical integrated applications, particularly for the first atmospheric window. It is emphasized that the performance of such hybrid photodetectors could be further improved by optimizing the interface and strengthening the hot carrier extraction. In addition, understanding the unrevealed hot carrier dynamics is particularly crucial for narrowing the gap between practical MIR systems and theoretical background-limited infrared performance (BLIP).

In summary, we have demonstrated that coupling 2D materials with plasmonic heavily doped metal oxides is an effective approach to achieving highly sensitive MIR photodetectors in the first atmo-

spheric windows of 3–5 μm. A plasmonic hot-electron-enabled MIR photodetector has been demonstrated on AZO/bi-layer graphene heterostructure. The device shows an ultrahigh detectivity of about 1.4×10^{11} Jones and high responsivity of about 4712.3 A/W under 3 μm at room temperature. The specific detectivity of this device is comparable with that of commercial state-of-the-art photodetectors and higher than that based on 2D materials in the MIR region. The sensitivity of the photodetectors is expected to be improved further by facilitating hot carrier extraction and delaying hot carrier cooling using phonon bottleneck or Auger heating effects.[36,37]

Acknowledgments. This work was supported by the National Key Research and Development Program of China (Grant No. 2017YFA0205700), the Strategic Priority Research Program of Chinese Academy of Sciences (Grant No. XDB30000000), the China Postdoctoral Science Foundation (Grant No. 2021M690625), and the Jiangsu Planned Projects for Postdoctoral Research Funds (Grant No. 2021K106B).

References

[1] Lu X W, Jiang P and Bao X H 2019 *Nat. Commun.* **10** 138
[2] Cao G Q, Wang F, Peng M, Shao X M, Yang B, Hu W D, Li X, Chen J, Shan Y B, Wu P S, Hu L G, Liu R, Gong H M, Cong C X and Qiu Z J 2020 *Adv. Electron. Mater.* **6** 1901007
[3] Wang Y, Gu Y, Cui A L, Li Q, He T, Zhang K, Wang Z, Li Z P, Zhang Z H, Wu P S, Xie R Z, Wang F, Wang P, Shan C X, Li H, Ye Z H, Zhou P and Hu W D 2022 *Adv. Mater.* **34** 2107772
[4] Lei W, Antoszewski J and Faraone L 2015 *Appl. Phys. Rev.* **2** 041303
[5] Xu J B, Hu J X, Wang R B, Li Q, Li W W, Guo Y F, Liu F K, Ullah Z, Wen L and Liu L W 2017 *Appl. Phys. Lett.* **111** 051106
[6] Xia F N, Wang H, Xiao D, Dubey M and Ramasubramaniam A 2014 *Nat. Photon.* **8** 899
[7] Yu Y F, Miao F, He J and Ni Z H 2017 *Chin. Phys. B* **26** 036801
[8] Fang H H and Hu W D 2017 *Adv. Sci.* **4** 1700323
[9] Zhang P, Zhang Y, Wang W H, Gao L, Li G F, Zhang S, Lu J P, Yu Y F and Zhang J L 2021 *Nanotechnology* **32** 415202
[10] Yu Y F, Li Z Z, Wang W H, Guo X T, Jiang J, Nan H Y and Ni Z H 2017 *J. Semicond.* **38** 033003
[11] Koppens F H, Mueller T, Avouris P, Ferrari A C, Vitiello M S and Polini M 2014 *Nat. Nanotechnol.* **9** 780
[12] Xia Y N and Halas N J 2005 *MRS Bull.* **30** 338
[13] Clavero C 2014 *Nat. Photon.* **8** 95
[14] Yu Y F and Ni Z H 2019 *Laser Optoelectron. Prog.* **56** 202403 (in Chinese)
[15] Wang W, Klots A, Prasai D, Yang Y, Bolotin K I and Valentine J 2015 *Nano Lett.* **15** 7440
[16] Calzolari A, Ruini A and Catellani A 2014 *ACS Photon.* **1** 703
[17] Lin J Y, Zhong K D and Lee P T 2016 *Opt. Express* **24** 5125
[18] Paria D, Vadakkumbatt V, Ravindra P, Avasthi S and Ghosh A 2021 *Nanotechnology* **32** 315202
[19] Aizpurua J, Bryant G W, Richter L J, de García A F J, Kelley B K and Mallouk T 2005 *Phys. Rev. B* **71** 235420
[20] Gu Y Y, Wang Y F, Xia J and Meng X M 2020 *Chin. Phys. Lett.* **37** 048101
[21] Brongersma M L, Halas N J and Nordlander P 2015 *Nat. Nanotechnol.* **10** 25
[22] Das A, Pisana S, Chakraborty B, Piscanec S, Saha S K, Waghmare U V, Novoselov K S, Krishnamurthy H R, Geim A K, Ferrari A C and Sood A K 2008 *Nat. Nanotechnol.* **3** 210
[23] Yan J, Zhang Y B, Kim P and Pinczuk A 2007 *Phys. Rev. Lett.* **98** 166802
[24] Ferrari A C 2007 *Solid State Commun.* **143** 47
[25] Wang F K, Zhang Y, Gao Y, Luo P, Su J W, Han W, Liu K L, Li H Q and Zhai T Y 2019 *Small* **15** 1901347
[26] Buscema M, Island J O, Groenendijk D J, Blanter S I, Steele G A, van der Zant H S and Castellanos-Gomez A 2015 *Chem. Soc. Rev.* **44** 3691
[27] Zhang M and Yeow J T W 2020 *Carbon* **156** 339
[28] Yan W, Shresha V R, Jeangros Q, Azar N S, Balendhran S, Ballif C, Crozier K and Bullock J 2020 *ACS Nano* **14** 13645
[29] Safaei A, Chandra S, Shabbir M W, Leuenberger M N and Chanda D 2019 *Nat. Commun.* **10** 3498
[30] Yu X, Li Y, Hu X, Zhang D, Tao Y, Liu Z, He Y, Haque M A, Liu Z, Wu T and Wang Q J 2018 *Nat. Commun.* **9** 4299
[31] Zeng L, Wu D, Jie J, Ren X, Hu X, Lau S P, Chai Y and Tsang Y H 2020 *Adv. Mater.* **32** 2004412
[32] Long M S, Gao A Y, Wang P, Xia H, Ott C, Pan C, Fu Y J, Liu E F, Chen X S, Lu W, Nilges T, Xu J B, XM W, Hu W D and Miao F 2017 *Sci. Adv.* **3** e1700589
[33] Ho V X, Wang Y, Cooney M P and Vinh N Q 2021 *Nanoscale* **13** 10526
[34] Ni Z Y, Ma L L, Du S C, Xu Y, Yuan M, Fang H H, Wang Z, Xu M S, Li D S, Yang J Y, Hu W D, Pi X D and Yang D R 2017 *ACS Nano* **11** 9854
[35] Chen Y F, Wang Y, Wang Z, Gu Y, Ye Y, Chai X L, Ye J F, Chen Y, Xie R Z, Zhou Y, Hu Z G, Li Q, Zhang L L, Wang F, Wang P, Miao J S, Wang J L, Chen X S, Lu W, Zhou P and Hu W D 2021 *Nat. Electron.* **4** 357
[36] Li M J, Fu J H, Xu Q and Sum T C 2019 *Adv. Mater.* **31** 1802486
[37] Li M J, Bhaumik S, Goh T W, Kumar M S, Yantara N, Gratzel M, Mhaisalkar S, Mathews N and Sum T C 2017 *Nat. Commun.* **8** 14350

Supporting Information for "Highly Sensitive Mid-Infrared Photodetector Enabled by Plasmonic Hot Carriers in the First Atmospheric Window"

Yuan-Fang Yu(于远方)[1], Ye Zhang(张也)[2], Fan Zhong(仲帆)[2], Lin Bai(白琳)[1], Hui Liu(刘辉)[2], Jun-Peng Lu(吕俊鹏)[1]* and Zhen-Hua Ni(倪振华)[1]*

[1]School of Physics, Southeast University, Nanjing 211189, China
[2]National Laboratory of Solid State Microstructures & School of Physics, Collaborative Innovation Center of Advanced Microstructures, Nanjing University, Nanjing 210093, China

1. Morphology of the fabricated AZO disc arrays

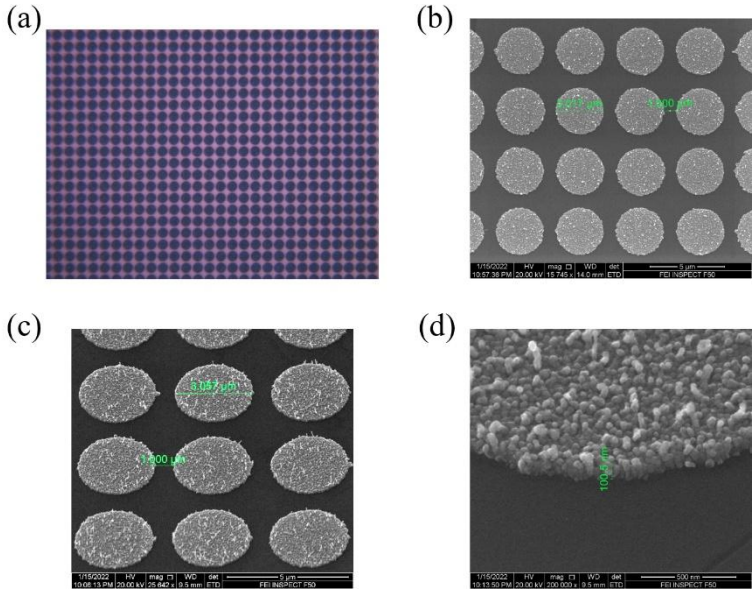

Fig. S1. (a) Optical image of AZO disc arrays on SiO_2/Si substrate. The diameter of AZO disc is 3μm. (b) SEM images AZO disc arrays on SiO_2/Si substrate with size measured. (c) SEM images AZO disc arrays observed along a certain tilt angle. (d) Thickness measurements of AZO disc.

2. The generation rate of hot electrons

The generation rate of hot electron is mainly relative to the energy of incident photons, electric field in nanostructures, and Fermi level. The generation rate of hot electrons can be calculated according to the equation below[1],

$$Rate_{HE} = \frac{2}{\pi^2} \times \frac{e^2 {E_F}^2}{\hbar} \frac{1}{(\hbar\omega)^3} \int_{S_{NC}} \left| E_{normal}(\theta, \varphi) \right|^2 ds \qquad \text{(S1)}$$

Where $E_{normal}(\theta, \varphi)$ is the component of electric field normal to the nanostructures' surface, inside the materials, and the integral is taken over the whole surface. E_F is the Fermi energy of AZO. $\hbar\omega$ is the photon energy.

3. Raman spectra of G band and 2D band

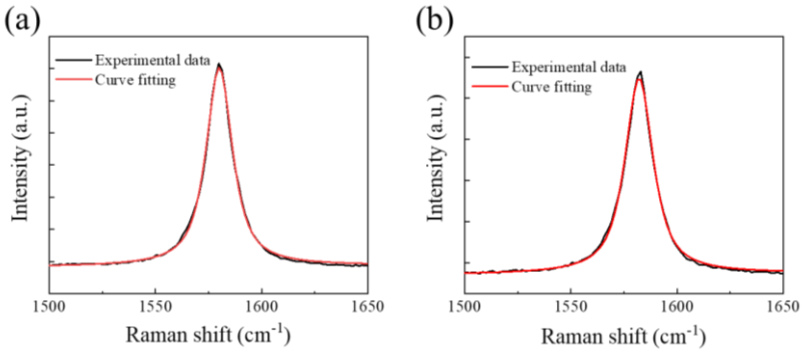

Fig. S2 (a) Raman G band of pristine bi-layer graphene, red line is the fitting curve of experimental data. (b) Raman G band of AZO/bi-layer graphene heterostructure, red line is the fitting curve of experimental data.

Table S1. Detail fitting results of the Raman G band for the bi-layer graphene and AZO/bi-layer graphene heterostructure

	Center (cm^{-1})	Width	Height
Bi-layer Graphene	1580	15	12367
AZO/bi-layer Graphene	1582	16	9514

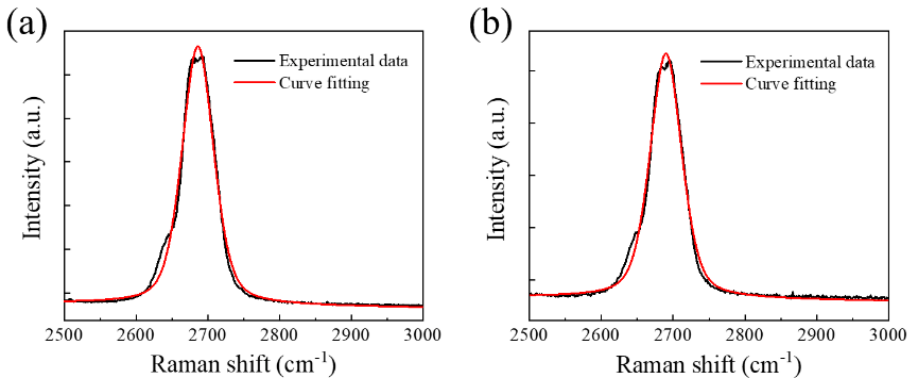

Fig. S3. (a) 2D band of pristine bi-layer graphene, red line is the fitting curve of experimental data. (b) 2D band of AZO/bi-layer graphene heterostructure, red line is the fitting curve of experimental data.

Table S2. Detail fitting results of the Raman 2D band for the bi-layer graphene and AZO/bi-layer graphene heterostructure

	Center (cm^{-1})	Width	Height
Bi-layer Graphene	2686	52	11845
AZO/bi-layer Graphene	2690	52	9372

4. Performance of AZO/bi-layer graphene photodetector at 3.5 μm and 4 μm, operated at room temperature

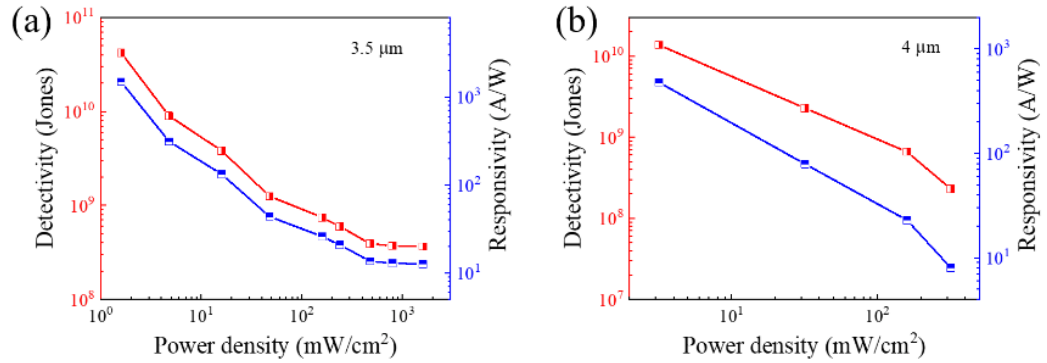

Fig. S4. (a) Detectivity and responsivity of AZO/bi-layer graphene photodetector as a function of power density at 3.5 μm. V_{ds} = 0.5 V, V_g = 0V. (b) Detectivity and responsivity of AZO/bi-layer graphene photodetector as a function of power density at 4 μm. V_{ds} = 0.5 V, V_g = 0V.

5. EQE of AZO/bi-layer graphene photodetector at room temperature

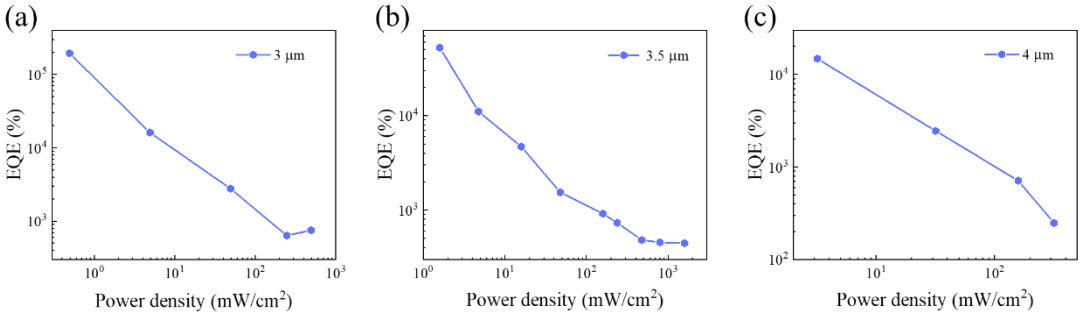

Fig. S5. EQE of AZO/bi-layer graphene photodetector as a function of power density at the wavelengths of 3 μm (a), 3.5 μm (b) and 4 μm (c). V_{ds} = 0.5 V, V_g = 0V.

Reference

[1] Liu T J, Besteiro L V, Wang Z M and Govorov A O 2019 *Faraday Discuss.* **214** 199